Tailoring electromagnetic responses in a coupled-grating system with combined modulation of near-field and far-field couplings

Feng Wu [1,*] Caifu Fan,[2] Kejia Zhu,[3] Jiaju Wu,[2] Xin Qi,[2] Yong Sun,[2] Shuyuan Xiao [4,5,†] Haitao Jiang,[2,‡] and Hong Chen[2]

[1]*School of Optoelectronic Engineering, Guangdong Polytechnic Normal University, Guangzhou 510665, China*

[2]*MOE Key Laboratory of Advanced Micro-Structured Materials, School of Physics Science and Engineering, Tongji University, Shanghai 200092, China*

[3]*Department of Electrical Engineering, Tongji University, Shanghai 201804, China*

[4]*Institute for Advanced Study, Nanchang University, Nanchang 330031, China*

[5]*Jiangxi Key Laboratory for Microscale Interdisciplinary Study, Nanchang University, Nanchang 330031, China*

(Received 13 April 2022; revised 29 May 2022; accepted 13 June 2022; published 27 June 2022)

Herein, we establish a hybrid coupling model (HCM) containing both near- and far-field couplings to describe the electromagnetic response of the coupled-grating system composed of two parallelly aligned subwavelength dielectric gratings. The HCM shows that the near-field coupling strength only contributes to the frequency splitting of two resonant modes, while the far-field one contributes to the frequency splitting and the linewidths of two resonant modes simultaneously. By changing the distance between two dielectric gratings, both the near- and far-field coupling strengths can be flexibly tuned, giving rise to rich electromagnetic responses. In addition, the formation of Fabry-Perot bound states in the continuum in coupled-grating systems can be clearly explained by the HCM. In this paper, we not only provide an all-dielectric platform for simultaneously manipulating near- and far-field couplings but also offer a viable approach to achieve reflectance/transmittance spectra with diverse shapes.

DOI: 10.1103/PhysRevB.105.245417

I. INTRODUCTION

Electromagnetic response tailoring (i.e., optical spectrum tailoring) has attracted the great interest of researchers since it plays a fundamental role in optical physics [1–4]. By tailoring electromagnetic responses, various optical functionalities (such as optical absorption, polarization manipulating, and lasing) with narrow bands [5–8], broad bands [9–12], and even multiple bands [13–15] can be achieved. Over the past several decades, optical resonators have been widely utilized to realize various optical functionalities with narrow bands [16–26]. To realize strong optical resonances, numerous microstructures have been proposed, such as photonic crystal cavities [16,17], microrings [18,19], split-ring resonators [20,21], metasurfaces [22–24], and subwavelength gratings [25,26]. Through coupling with optical resonators, electromagnetic responses can be tailored flexibly [27,28]. Such couplings can be divided into two classes: near- and far-field couplings. On one hand, near-field couplings can be realized in coupled microrings [29] (or microtoroid [30]), coupled split-ring resonators [31,32], and dielectric disk chains [33]. Through exploring near-field couplings, researchers found a series of interesting physical phenomena, including exceptional points [34–36], electromagnetically induced transparency [37,38], and plasmon-induced transparency [39,40]. On the other hand, far-field couplings can be realized in waveguide-coupled resonators [41–44] and metamaterial crystals [45]. Through exploring far-field couplings, researchers also found a series of interesting physical phenomena, including Fano resonances [42,43] and topological phase transition [43,45]. Additionally, waveguide-coupled resonators in the weak-coherent regime have also been utilized to reveal the nontrivial photon propagation and scattering characteristics [46,47]. Interestingly, researchers found that near- and far-field couplings can coexist in some special coupled-resonators systems, which greatly enriches the electromagnetic response tailoring [48–52]. To reveal the underlying physics of near- and far-field optical losses, researchers proposed first-principles-based physical models of photonic radiative [53] and absorption losses [54]. Only a few metallic coupled-resonators systems can support near- and far-field couplings simultaneously [48–52].

Over the past two decades, subwavelength dielectric gratings have attracted immense interest due to their unique resonant properties [55–57]. Owing to the guided mode resonances (GMRs), subwavelength dielectric gratings can be viewed as narrow-band resonators [55–57]. In this paper, we parallelly align two identical subwavelength dielectric gratings separated by air to constitute a coupled-grating system. Within the framework of the temporal coupled-mode theory (TCMT) [58], we establish a hybrid coupling model (HCM) containing both near- and far-field couplings to describe the electromagnetic response of the coupled-grating system. The near-field coupling originates from the overlapping of strongly localized evanescent waves of two gratings.

*fengwu@gpnu.edu.cn
†syxiao@ncu.edu.cn
‡jiang-haitao@tongji.edu.cn

 ©2022 American Physical Society

The origination of the far-field coupling can be explained as follows. One of the grating couples to the incident electromagnetic wave and then reradiates a propagating wave (details can be seen in Sec. II A). The reradiative propagating wave undergoes the distance between two gratings and finally couples with the other grating. This coupling is related to the phase of the propagating wave between two gratings and the so-called far-field coupling. The cooccurrence of the near- and far-field couplings enables us to achieve rich electromagnetic responses which cannot be obtained in the systems where only one kind of coupling exists. The proposed HCM shows that the near-field coupling strength only contributes to the frequency splitting of two resonant modes, while the far-field one contributes to the frequency splitting and the linewidths of two resonant modes simultaneously. By changing the distance between two gratings, both the near- and far-field coupling strengths can be flexibly tuned. Additionally, the proposed HCM can explain the formation of Fabry-Perot bound states in the continuum (BICs) in coupled-grating systems [59–62]. In this paper, we not only provide an all-dielectric platform for simultaneously manipulating near- and far-field couplings but also offer a viable approach to achieve reflectance/transmittance spectra with diverse shapes.

This paper is organized as follows. In Sec. II, we establish a HCM containing both near- and far-field couplings for the coupled-grating system within the framework of the TCMT. First, the dynamic equations of the coupled-grating system are given in Sec. II A. Second, the reflectance of the coupled-grating system is derived in Sec. II B. Third, two complex eigenfrequencies of the coupled-grating system are solved in Sec. II C. In Sec. III, we give the numerical results and discussions to confirm the correctness of the proposed theoretical model. Specifically, the numerical results of the coupled-grating systems when two gratings are close and far away are given in Secs. III A and III B, respectively. Next, the mechanism of the Fabry-Perot BICs in the coupled-grating system is analyzed in Sec. III C. Finally, the conclusion is given in Sec. IV.

II. HCM CONTAINING BOTH NEAR- AND FAR-FIELD COUPLINGS FOR COUPLED-GRATING SYSTEMS

In this section, we establish a HCM containing both near- and far-field couplings for coupled-grating systems. In Sec. II A, we give the dynamic equations of the coupled-grating system within the framework of the TCMT [58]. Then the reflectance of the coupled-grating system is derived in Sec. II B. Finally, to obtain the angular frequency positions and the corresponding linewidths of two resonant modes, we solve two complex eigenfrequencies of the coupled-grating system in Sec. II C.

A. Dynamic equations of coupled-grating systems

Figure 1(a) shows the schematic of the coupled-grating system composed of two parallelly aligned identical subwavelength gratings. For each grating, the refractive indices of the high- and low-index media are n_H and n_L, respectively. The grating constant is denoted by Λ, the duty cycle is denoted by p, and the height is denoted by h. The distance between two identical gratings is denoted by d. Around the angular frequency of the GMR, the electromagnetic response of each grating can be described by the single resonator model (SRM) [63]. Therefore, the electromagnetic response of the coupled-grating system can be described by a coupled-resonator system composed of two resonators.

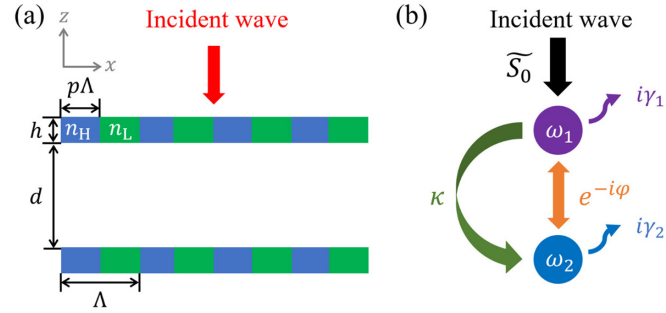

FIG. 1. (a) Schematic of the coupled-grating system composed of two parallelly aligned identical subwavelength gratings. (b) Hybrid coupling model (HCM) containing both near- and far-field couplings, which describes the electromagnetic response of the coupled-grating system.

We establish a HCM containing both near- and far-field couplings to describe the electromagnetic response of the coupled-grating system, as schematically shown in Fig. 1(b). The resonant angular frequencies of two resonators are denoted by ω_1 and ω_2, respectively. The radiative losses of two resonators are denoted by γ_1 and γ_2, respectively. Supposing an electromagnetic wave $\widetilde{S}_0$ normally impinges on the coupled-grating system, the dynamic equations for two resonance modes ($\widetilde{a}_1$ and $\widetilde{a}_2$) can be determined by the TCMT [58]:

$$\frac{d\widetilde{a}_1}{dt} = (i\omega_1 - \gamma_1)\widetilde{a}_1 + i\kappa\widetilde{a}_2 + i\sqrt{\gamma_1}\widetilde{S}_0 + i\sqrt{\gamma_1}(i\sqrt{\gamma_2}e^{-i\varphi}\widetilde{a}_2), \tag{1a}$$

$$\frac{d\widetilde{a}_2}{dt} = (i\omega_2 - \gamma_2)\widetilde{a}_2 + i\kappa\widetilde{a}_1 + i\sqrt{\gamma_2}e^{-i\varphi}\widetilde{S}_0 + i\sqrt{\gamma_2}(i\sqrt{\gamma_1}e^{-i\varphi}\widetilde{a}_1). \tag{1b}$$

In the right-hand side of Eq. (1a), the second term $i\kappa\widetilde{a}_2$ represents the near-field interaction between two resonators with the near-field coupling strength κ. The near-field coupling originates from the overlapping of strongly localized evanescent waves of two resonators. The third term $i\sqrt{\gamma_1}\widetilde{S}_0$ represents the direct coupling between the incident electromagnetic wave $\widetilde{S}_0$ and resonator 1 [64]. The fourth term $i\sqrt{\gamma_1}(i\sqrt{\gamma_2}e^{-i\varphi}\widetilde{a}_2)$ can be explained as follows. When the incident electromagnetic wave $\widetilde{S}_0$ normally impinges on the coupled-resonator system, resonator 2 will reradiate a propagating wave $i\sqrt{\gamma_2}\widetilde{a}_2$. The reradiative propagating wave undergoes the distance between two resonators d with the phase $\varphi = k_0 d$ and finally couples with resonator 1. Hence, the fourth term can be expressed as $i\sqrt{\gamma_1}(i\sqrt{\gamma_2}e^{-i\varphi}\widetilde{a}_2)$. The second, third, and fourth terms in the right-hand side of Eq. (1b) can be explained similarly.

Then Eqs. (1a) and (1b) can be reduced as

$$\frac{d\widetilde{a_1}}{dt} = (i\omega_1 - \gamma_1)\widetilde{a_1} + i\kappa\widetilde{a_2} + i\sqrt{\gamma_1}\widetilde{S_0} - \sqrt{\gamma_1\gamma_2}e^{-i\varphi}\widetilde{a_2}, \quad (2a)$$

$$\frac{d\widetilde{a_2}}{dt} = (i\omega_2 - \gamma_2)\widetilde{a_2} + i\kappa\widetilde{a_1} + i\sqrt{\gamma_2}e^{-i\varphi}\widetilde{S_0} - \sqrt{\gamma_1\gamma_2}e^{-i\varphi}\widetilde{a_1}. \quad (2b)$$

One can clearly see that the far-field coupling strength is $\sqrt{\gamma_1\gamma_2}e^{-i\varphi}$. One of the resonators couples to the incident electromagnetic wave and then reradiates a propagating wave. The reradiative propagating wave undergoes the distance between two resonators and finally couples with the other resonator. This coupling is related to the phase of the propagating wave between two resonators and the so-called far-field coupling.

In the coupled-grating system shown in Fig. 1(a), the two subwavelength gratings are identical. Hence, we have $\omega_1 = \omega_2 = \omega_0$ and $\gamma_1 = \gamma_2 = \gamma_0$. As a result, Eqs. (2a) and (2b) can be further reduced to

$$\frac{d\widetilde{a_1}}{dt} = (i\omega_0 - \gamma_0)\widetilde{a_1} + i\kappa\widetilde{a_2} + i\sqrt{\gamma_0}\widetilde{S_0} - \gamma_0 e^{-i\varphi}\widetilde{a_2}, \quad (3a)$$

$$\frac{d\widetilde{a_2}}{dt} = (i\omega_0 - \gamma_0)\widetilde{a_2} + i\kappa\widetilde{a_1} + i\sqrt{\gamma_0}e^{-i\varphi}\widetilde{S_0} - \gamma_0 e^{-i\varphi}\widetilde{a_2}. \quad (3b)$$

The far-field coupling strength now becomes $\gamma_0 e^{-i\varphi}$. Considering the time harmonic case, we have

$$\widetilde{a_k} = A_k e^{i\omega t} \quad (k = 1,\ 2), \quad (4a)$$

$$\widetilde{S_0} = S_0 e^{i\omega t}, \quad (4b)$$

where ω represents the angular frequency, and t represents the time. Under the steady-state condition $(dA_k/dt = 0)$, Eqs. (3a) and (3b) can be reduced to

$$[i(\omega_0 - \omega) - \gamma_0]A_1 + (i\kappa - \gamma_0 e^{-i\varphi})A_2 + i\sqrt{\gamma_0}S_0 = 0, \quad (5a)$$

$$(i\kappa - \gamma_0 e^{-i\varphi})A_1 + [i(\omega_0 - \omega) - \gamma_0]A_2 + i\sqrt{\gamma_0}e^{-i\varphi}S_0 = 0. \quad (5b)$$

After some algebra, we can finally obtain the solutions of Eqs. (5a) and (5b):

$$A_1 = \frac{i\sqrt{\gamma_0}e^{-i\varphi}(i\kappa - \gamma_0 e^{-i\varphi}) - i\sqrt{\gamma_0}[i(\omega_0 - \omega) - \gamma_0]}{[i(\omega_0 - \omega) - \gamma_0]^2 - (i\kappa - \gamma_0 e^{-i\varphi})^2}S_0, \quad (6a)$$

$$A_2 = \frac{i\sqrt{\gamma_0}(i\kappa - \gamma_0 e^{-i\varphi}) - i\sqrt{\gamma_0}e^{-i\varphi}[i(\omega_0 - \omega) - \gamma_0]}{[i(\omega_0 - \omega) - \gamma_0]^2 - (i\kappa - \gamma_0 e^{-i\varphi})^2}S_0. \quad (6b)$$

B. Reflectance of coupled-grating systems

According to the TCMT [58], the reflection coefficient of the coupled-grating system can be expressed as

$$r(\omega, \omega_0, \gamma_0, \kappa, \varphi) = \frac{i\sqrt{\gamma_0}A_1 + i\sqrt{\gamma_0}e^{-i\varphi}A_2}{S_0}. \quad (7)$$

It should be noted that the reflection coefficient is a function of five variables ω, ω_0, γ_0, κ, and φ. Then the reflectance of the coupled-grating system can be given by

$$R(\omega, \omega_0, \gamma_0, \kappa, \varphi) = |r(\omega, \omega_0, \gamma_0, \kappa, \varphi)|^2 = \left|\frac{i\sqrt{\gamma_0}A_1 + i\sqrt{\gamma_0}e^{-i\varphi}A_2}{S_0}\right|^2. \quad (8)$$

Similarly, the reflectance is a function of five variables ω, ω_0, γ_0, κ, and φ.

C. Two complex eigenfrequencies of coupled-grating systems

To obtain the angular frequency positions and the corresponding linewidths of two resonant modes, we solve two complex eigenfrequencies of the coupled-grating system. To solve the eigenvalue problem, the coupled-grating system should be viewed as a closed system, i.e., $S_0 = 0$ [29]. Then rewriting Eqs. (5a) and (5b) in the matrix form, we obtain

$$\begin{bmatrix} i(\omega_0 - \omega) - \gamma_0 & i\kappa - \gamma_0 e^{-i\varphi} \\ i\kappa - \gamma_0 e^{-i\varphi} & i(\omega_0 - \omega) - \gamma_0 \end{bmatrix}\begin{pmatrix} A_1 \\ A_2 \end{pmatrix} = \begin{pmatrix} 0 \\ 0 \end{pmatrix}. \quad (9)$$

Equation (9) possesses nontrivial solutions when

$$\begin{vmatrix} i(\omega_0 - \omega) - \gamma_0 & i\kappa - \gamma_0 e^{-i\varphi} \\ i\kappa - \gamma_0 e^{-i\varphi} & i(\omega_0 - \omega) - \gamma_0 \end{vmatrix} = 0. \quad (10)$$

Two complex eigenfrequencies can be obtained:

$$\begin{aligned}\omega_\pm &= \omega_0 \pm \kappa + i\gamma_0(1 \pm e^{-i\varphi}) \\ &= \omega_0 \pm (\kappa + \gamma_0 \sin\varphi) \\ &\quad + i\gamma_0(1 \pm \cos\varphi).\end{aligned} \quad (11)$$

The angular frequency positions of two resonant modes are determined by the real parts of two complex eigenfrequencies:

$$\mathrm{Re}(\omega_\pm) = \omega_0 \pm (\kappa + \gamma_0 \sin\varphi). \quad (12a)$$

Hence, the angular frequency positions of two resonant modes are determined by both the near- and far-field coupling strengths (κ and $\gamma_0 e^{-i\varphi}$). The corresponding linewidths of two resonant modes are determined by the imaginary parts of two complex eigenfrequencies:

$$\mathrm{Im}(\omega_\pm) = \gamma_0(1 \pm \cos\varphi). \quad (12b)$$

Hence, the linewidths of two resonant modes are completely determined by the far-field coupling strength ($\gamma_0 e^{-i\varphi}$). Finally, the Q factors of two resonant modes can be calculated by

$$Q_\pm = \frac{1}{2}\frac{\mathrm{Re}(\omega_\pm)}{\mathrm{Im}(\omega_\pm)} = \frac{\omega_0 \pm (\kappa + \gamma_0 \sin\varphi)}{2\gamma_0(1 \pm \cos\varphi)}. \quad (13)$$

The values of ω_0 and γ_0 can be obtained by fitting the reflectance spectrum of the single grating by the SRM [63]. When the distance between two gratings d varies, both the near- and far-field coupling strengths (κ and $\gamma_0 e^{-i\varphi}$) will change. According to Eqs. (12a) and (12b), both the angular frequency positions and the linewidths of two resonant modes of the coupled-grating system can be flexibly tuned. In other words, by changing the distance between two gratings, the coupled-grating system exhibits rich spectral shapes.

Interestingly, the formation of Fabry-Perot BICs [59–62] can be clearly explained by Eq. (13).

III. NUMERICAL RESULTS AND DISCUSSIONS

In this section, we demonstrate the theoretical model established in Sec. II by fitting the reflectance spectrum calculated by the rigorous coupled-wave analysis (RCWA) [65] using Eq. (8). The RCWA has been widely utilized to directly obtain the electromagnetic responses of gratings. It is a conventional approach to calculate exact solutions of Maxwell's equations for the electromagnetic diffractions by gratings [65]. In the RCWA, both the permittivity functions and the electromagnetic fields are expanded into Fourier series for each layer [66]. Then the boundary-value problem can be reduced to an algebraic eigenvalue problem [66]. Finally, connecting the solutions of the electromagnetic fields at the layer interfaces by the continuity of the tangential components of the electromagnetic fields, the diffraction efficiencies of each order of the reflected and the transmitted waves can be obtained [65]. The accuracy of the solutions depends solely on the number of terms retained in the space-harmonic expansions of the electromagnetic fields [65]. In our calculations, the number of terms retained in the space-harmonic expansions of the electromagnetic fields is set to be 11 to guarantee the accuracy of the solutions. In Sec. III A, we give the numerical results of the coupled-grating systems when two gratings are close (i.e., $\kappa > \gamma_0$). Then we give the numerical results when two grating are far away (i.e., $\kappa < \gamma_0$) in Sec. III B. Finally, the mechanism of Fabry-Perot BICs in the coupled-grating system is analyzed in Sec. III C.

First, we obtain the values of ω_0 and γ_0 by fitting the reflectance spectrum of the single grating by the SRM. For the single grating, the refractive indices of the high- and low-index media are set to be $n_H = 2$ and $n_L = 1.6$, respectively. The geometric parameters are selected to be $\Lambda = 333$ nm, $p = 0.5$, and $h = 134$ nm. The surrounding medium is selected to be air. According to the RCWA [65], we calculate the reflectance spectrum (zero-order diffraction) of the single grating for transverse electric (TE) polarization at normal incidence, as shown by the blue solid line in Fig. 2. According to the SRM [63], the reflectance can be expressed as

$$R(\omega, \omega_0, \gamma_0) = \frac{\gamma_0^2}{(\omega_0 - \omega)^2 - \gamma_0^2}. \tag{14}$$

By fitting the reflectance spectrum by the SRM (see the red dashed line in Fig. 2), the values of $\omega_0 = 3.8172 \times 10^{15}$ Hz and $\gamma_0 = 0.0285 \times 10^{15}$ Hz can be obtained. It should be noted that Eq. (14) describes a symmetric Lorentz line shape. According to the GMR mechanism, resonant peaks of subwavelength grating usually exhibit asymmetric Fano line shapes [55–57]. To better fit the reflectance spectrum of the subwavelength grating by the SRM, we select the proper values of the refractive indices and the geometric parameters of the subwavelength grating. In addition, the values of the refractive indices (n_H and n_L) and the geometric parameters (Λ, p, and h) of the subwavelength grating determine the resonant angular frequency of the subwavelength grating resonator ω_0 and the radiative loss of the subwavelength grating resonator γ_0 in the HCM [Eqs. (3a) and (3b)].

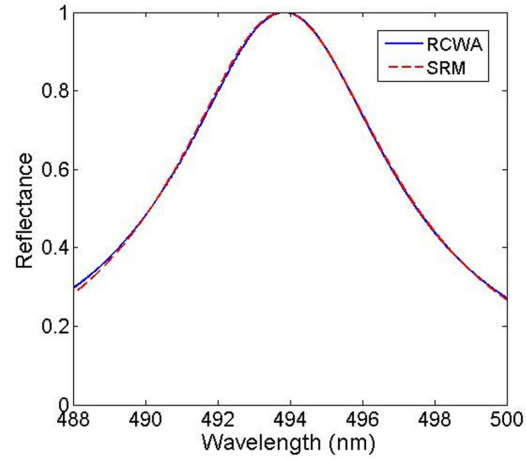

FIG. 2. Reflectance spectrum of the single subwavelength grating for transverse electric (TE) polarization at normal incidence. Blue solid line represents the reflectance spectrum calculated by the rigorous coupled-wave analysis (RCWA). Red dashed line represents the fitting reflectance spectrum based on the single resonator model (SRM).

A. Numerical results of coupled-grating systems when two gratings are close ($\kappa > \gamma_0$)

When two grating are close, two gratings are coupled strongly. When the near-field coupling strength between two gratings κ is larger than the radiative loss of the single grating γ_0 (i.e., $\kappa > \gamma_0$), we define two gratings are close. We select the distances between two gratings as $d = 100$, 140, and 180 nm. According to the RCWA, we calculate the corresponding reflectance spectra (zero-order diffraction) of the coupled-grating systems for TE polarization at normal incidence, as shown by the blue solid lines in Figs. 3(a)–3(c). The corresponding fitted reflectance spectra based on the HCM [Eq. (8)] are also shown by the red dashed lines. One can see that the reflectance spectra predicted by the HCM basically agree with those calculated by the RCWA. For $d = 100$, 140, and 180 nm, the fitted near- and far-field coupling strengths are ($\kappa = 0.0969 \times 10^{15}$ Hz, $\gamma_0 e^{-i\varphi} = \gamma_0 e^{-0.293\pi i}$), ($\kappa = 0.0557 \times 10^{15}$ Hz, $\gamma_0 e^{-i\varphi} = \gamma_0 e^{-0.570\pi i}$), and ($\kappa = 0.0345 \times 10^{15}$ Hz, $\gamma_0 e^{-i\varphi} = \gamma_0 e^{-0.795\pi i}$), respectively.

Since $\kappa > \gamma_0$, the angular frequency splitting of two resonant modes $\Delta\omega = \omega_+ - \omega_-$ is mainly determined by the near-field coupling strength κ, according to Eq. (12a). As the distance between two gratings d increases, the near-field coupling strength κ decreases. Therefore, the angular splitting of two resonant modes $\Delta\omega$ becomes smaller. The linewidths of two resonant modes $\Delta\omega_+$ and $\Delta\omega_-$ can be flexibly tuned by the far-field coupling strength $\gamma_0 e^{-i\varphi}$, according to Eq. (12b). As the distance between two gratings d increases, the phase within the far-field coupling strength φ increases. Therefore, the linewidth of the high-frequency resonant mode $\Delta\omega_+$ becomes smaller, while that of the low-frequency resonant mode $\Delta\omega_-$ becomes larger.

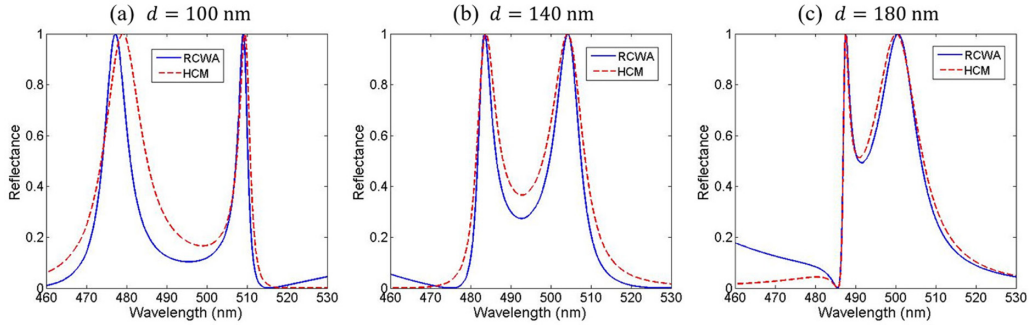

FIG. 3. Reflectance spectra of the coupled-grating systems with different distances between two gratings (a) $d = 100$ nm, (b) $d = 140$ nm, and (c) $d = 180$ nm for transverse electric (TE) polarization at normal incidence. Blue solid lines represent the reflectance spectra calculated by the rigorous coupled-wave analysis (RCWA). Red dashed lines represent the fitting reflectance spectra based on the hybrid coupling model (HCM).

It is known that the near-field coupling strength κ is linearly dependent on $e^{-k_0 d}$ in the coupled split-ring resonators [31]. Here, we confirm that it is also verified in the coupled-grating system since it is determined by the overlapping evanescent fields of two gratings. We select 11 cases of distance d in total, ranging from 100 to 200 nm with a step of 10 nm. For these 11 cases, we can obtain 11 fitted near-field coupling strengths κ. The values of $e^{-k_0 d}$ and the corresponding fitted κ are shown by the blue circles in Fig. 4. The linear fitting line is also given by the red dashed line. The near-field coupling strength κ is nearly proportional to $e^{-k_0 d}$.

B. Numerical results of coupled-grating systems when two gratings are far away ($\kappa < \gamma_0$)

When two grating are far away, two gratings are not coupled strongly. When the near-field coupling strength between two gratings κ is smaller than the radiative loss of a single grating γ_0 (i.e., $\kappa < \gamma_0$), we define two gratings are far away. We select the distances between two gratings as $d = 280$, 320, and 360 nm. According to the RCWA, we calculate the corresponding reflectance spectra (zero-order diffraction) of the coupled-grating systems for TE polarization at normal incidence, as shown by the blue solid lines in Figs. 5(a)–5(c). The corresponding fitted reflectance spectra based on the HCM [Eq. (8)] are also shown by the red dashed lines. Clearly, the reflectance spectra predicted by the HCM basically agree with those calculated by the RCWA. For $d = 280$, 320, and 360 nm, the fitted near- and far-field coupling strengths are ($\kappa = 0.0069 \times 10^{15}$ Hz, $\gamma_0 e^{-i\varphi} = \gamma_0 e^{-1.114\pi i}$), ($\kappa = 0.0042 \times 10^{15}$ Hz, $\gamma_0 e^{-i\varphi} = \gamma_0 e^{-1.261\pi i}$), and ($\kappa = 0.0042 \times 10^{15}$ Hz, $\gamma_0 e^{-i\varphi} = \gamma_0 e^{-1.451\pi i}$), respectively.

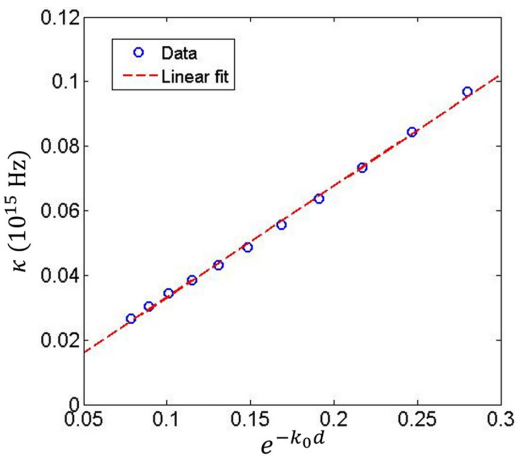

FIG. 4. Dependence of the near-field coupling strength κ on the $\exp(-k_0 d)$. Red dashed line represents the linear fitting line.

Since $\kappa < \gamma_0$, the two resonant modes ω_+ and ω_- are almost degenerated, according to Eq. (12a). The linewidths of two resonant modes $\Delta\omega_+$ and $\Delta\omega_-$ can be flexibly tuned by the far-field coupling strength $\gamma_0 e^{-i\varphi}$, according to Eq. (12b). As shown in Fig. 5, these two almost generated resonant modes with different linewidths greatly enrich the line shape of the reflectance spectrum of the coupled-grating system.

For a normally propagating electromagnetic wave, the propagating phase between two gratings can be expressed as $k_0 d$. As we discussed in Sec. II A, the phase term of the far-field coupling strength can be expressed as $\varphi = k_0 d$ in the coupled-grating system. To confirm this relationship, we select 11 cases of distance d in total, ranging from 320 to 420 nm with a step of 10 nm. For these 11 cases, we can obtain 11 fitted phase terms of the far-field coupling strengths φ. The values of d and the corresponding fitted φ are shown by the blue circles in Fig. 6. The relationship $\varphi = k_0 d$ is also given by the red dashed line. The fitted φ is quite close to the $k_0 d$.

C. Mechanism of Fabry-Perot BICs

According to Eq. (12b), the linewidths of two resonant modes $\Delta\omega_+$ and $\Delta\omega_-$ are completely determined by the far-field coupling strength ($\gamma_0 e^{-i\varphi}$). According to Eq. (13), the Q factor of the resonant mode becomes infinite when $\cos\varphi = \pm 1$. Now we discuss these two cases, respectively.

When $\varphi = (2m+1)\pi$ ($m \in N$), the complex eigenfrequency of the resonant mode ω_+ can be given by

$$\omega_+ = \omega_0 + \kappa. \tag{15a}$$

The corresponding Q factor can be calculated by

$$Q_+ = \frac{1}{2}\frac{\mathrm{Re}(\omega_+)}{\mathrm{Im}(\omega_+)} \to \infty. \tag{15b}$$

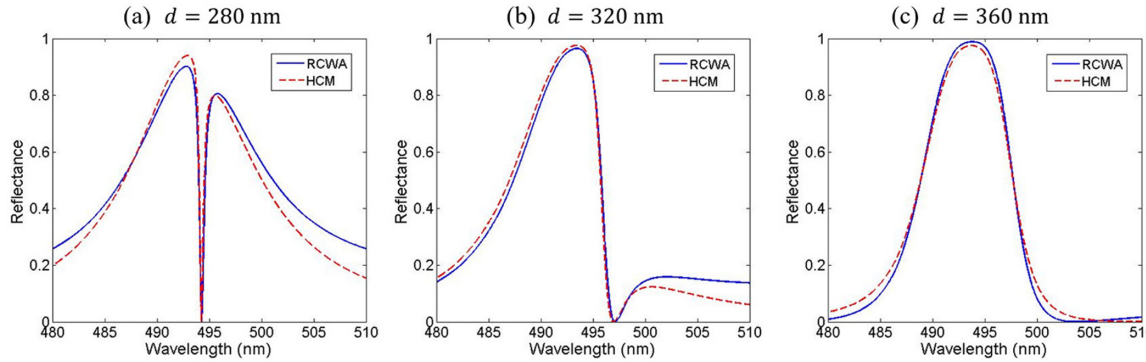

FIG. 5. Reflectance spectra of the coupled-grating systems with different distances between two gratings (a) $d = 280$ nm, (b) $d = 320$ nm, and (c) $d = 360$ nm for transverse electric (TE) polarization at normal incidence. Blue solid lines represent the reflectance spectra calculated by the rigorous coupled-wave analysis (RCWA). Red dashed lines represent the fitting reflectance spectra based on the hybrid coupling model (HCM).

Interestingly, the Q factor of the resonant mode Q_+ reaches infinite, which corresponds to a BIC. The round-trip phase shift between two gratings is $2\varphi = (2m+1)2\pi$. Hence, this type of BIC is also called the Fabry-Perot BIC [59–62].

Similarly, the complex eigenfrequency of the resonant mode ω_- can be given by

$$\omega_- = \omega_0 - \kappa + i2\gamma_0. \tag{16a}$$

The corresponding Q factor can be calculated by

$$Q_- = \frac{1}{2}\frac{\mathrm{Re}(\omega_-)}{\mathrm{Im}(\omega_-)} = \frac{\omega_0 - \kappa}{4\gamma_0}. \tag{16b}$$

To investigate this BIC, we select the distances between two gratings as $d = 180$, 200, and 220 nm. The corresponding phase shift between two gratings are $k_0 d = 0.729\pi$, 0.810π, and 0.891π, respectively. According to the RCWA, we calculate the corresponding reflectance spectra (zero-order diffraction) of the coupled-grating systems for TE polarization at normal incidence, as shown by the blue solid lines in Figs. 7(a)–7(c). The corresponding fitted reflectance spectra based on the HCM [Eq. (8)] are also shown by the red dashed lines. As demonstrated, the reflectance spectra predicted by the HCM basically agree with those calculated by the RCWA. For $d = 180$, 200, and 220 nm, the fitted near- and far-field coupling strengths are ($\kappa = 0.0345 \times 10^{15}$ Hz, $\gamma_0 e^{-i\varphi} = \gamma_0 e^{-0.795\pi i}$), ($\kappa = 0.0267 \times 10^{15}$ Hz, $\gamma_0 e^{-i\varphi} = \gamma_0 e^{-0.868\pi i}$), and ($\kappa = 0.0199 \times 10^{15}$ Hz, $\gamma_0 e^{-i\varphi} = \gamma_0 e^{-0.932\pi i}$), respectively. The reflectance spectra around the resonant modes ω_+ exhibit asymmetric Fano line types. Hence, the corresponding Q factor can be calculated by $Q_+ = \omega_{\mathrm{Dip}}/(\omega_{\mathrm{Dip}} - \omega_{\mathrm{Peak}})$, where ω_{Dip} and ω_{Peak} represent the angular frequencies at the reflectance dip and peak, respectively [67]. As the phase shift gradually increases from 0.729π to 0.891π, the Q factor of the resonant mode Q_+ rapidly increases from 2.4×10^2 to 2.2×10^3. Using the finite-difference time-domain (FDTD) method via commercial software package Lumerical FDTD Solutions, we simulate the electric field intensity distributions $|E_y|$ at the corresponding reflectance dips (A–C), as respectively shown in Figs. 7(d)–7(f). The incident electric field intensity is set to be unity, i.e., $|E_y^{\mathrm{inc}}| = 1$. One can see that the electric field is greatly enhanced within the gratings. As the phase shift gradually increases from 0.729π to 0.891π, the maximum electric field intensity rapidly increases from $\sim$6 to $\sim$25, which indicates that the strength of the resonance increases dramatically.

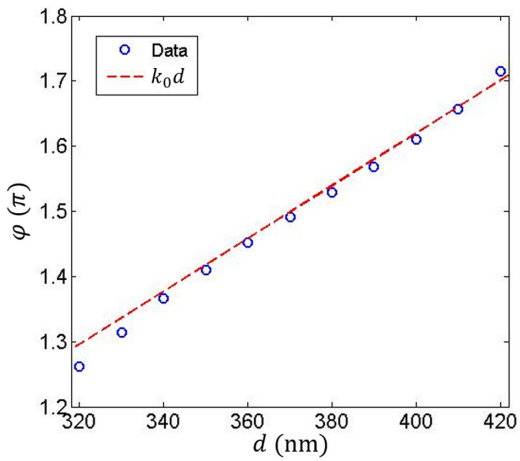

FIG. 6. Dependence of the phase term of the far-field coupling strength φ on the distance d. Red dashed line represents the relationship $\varphi = k_0 d$.

Then we give the dependence of the Q factor of the resonant mode Q_+ on the phase shift $k_0 d$, as shown in Fig. 8. One can clearly see that, as the phase shift approaches π, the Q factor increases dramatically. For example, the Q factor reaches 7.6×10^5 when the phase shift is 0.980π. Therefore, the Q factor becomes infinite when the phase shift is equal to π, which is consistent with the theoretical prediction of Eq. (15b).

When $\varphi = 2m\pi$ ($m \in N$), the complex eigenfrequency of the resonant mode ω_+ can be given by

$$\omega_+ = \omega_0 + \kappa + i2\gamma_0. \tag{17a}$$

The corresponding Q factor can be calculated by

$$Q_+ = \frac{1}{2}\frac{\mathrm{Re}(\omega_+)}{\mathrm{Im}(\omega_+)} = \frac{\omega_0 + \kappa}{4\gamma_0}. \tag{17b}$$

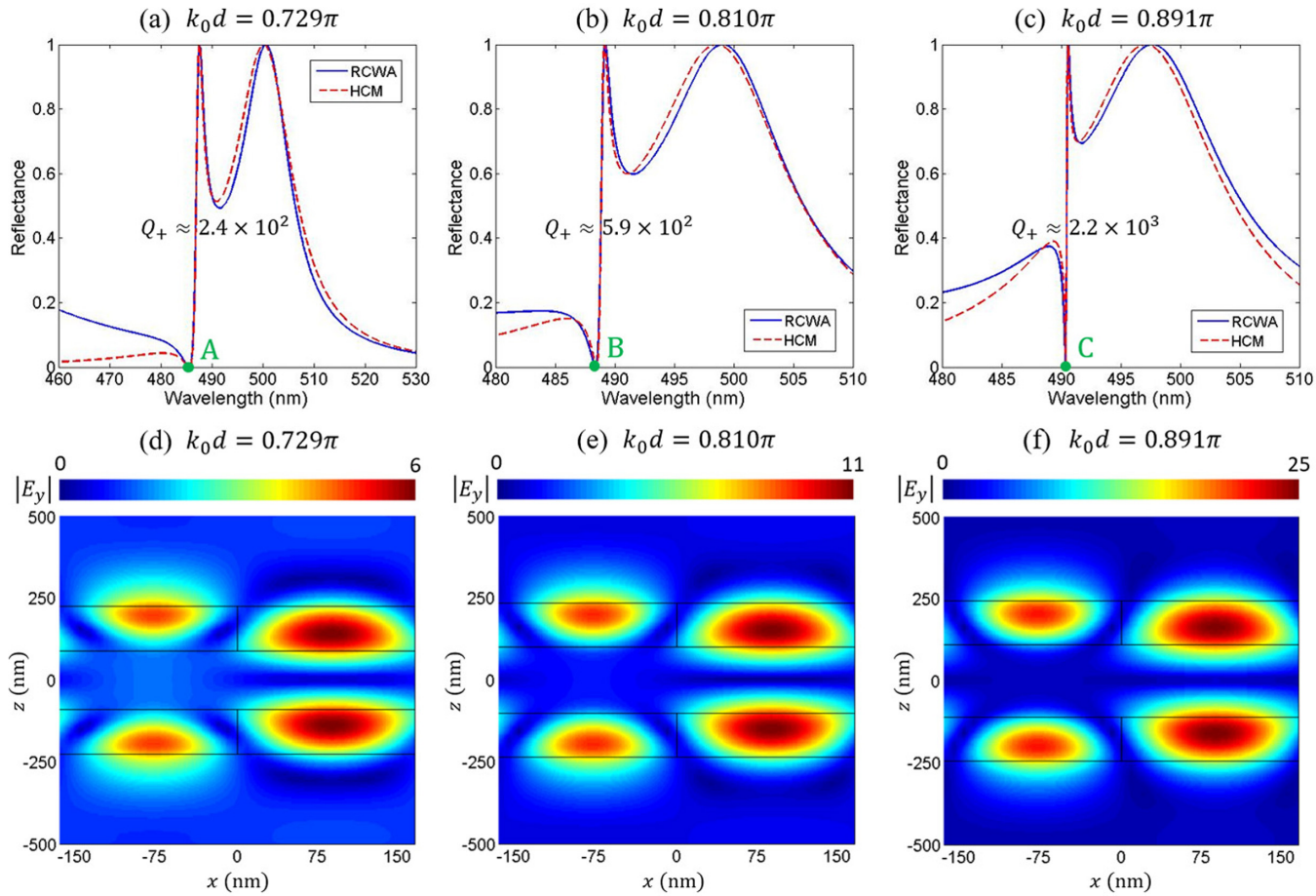

FIG. 7. Reflectance spectra of the coupled-grating systems with phase shifts between two gratings (a) $k_0d = 0.729\pi$, (b) $k_0d = 0.810\pi$, and (c) $k_0d = 0.891\pi$ for transverse electric (TE) polarization at normal incidence. Blue solid lines represent the reflectance spectra calculated by the rigorous coupled-wave analysis (RCWA). Red dashed lines represent the fitting reflectance spectra based on the hybrid coupling model (HCM). (d)–(f) Electric field intensity distributions $|E_y|$ at the corresponding reflectance dips (A–C). The incident electric field intensity is set to be unity, i.e., $|E_y^{\text{inc}}| = 1$.

Similarly, the complex eigenfrequency of the resonant mode ω_- can be given by

$$\omega_- = \omega_0 - \kappa. \tag{18a}$$

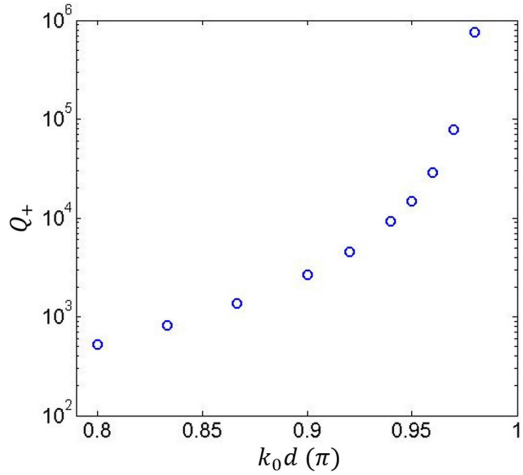

FIG. 8. Dependence of the Q factor of the resonant mode Q_+ on the phase shift between two gratings k_0d.

The corresponding Q factor can be calculated by

$$Q_- = \frac{1}{2}\frac{\text{Re}(\omega_-)}{\text{Im}(\omega_-)} \to \infty. \tag{18b}$$

The Q factor of the resonant mode Q_- reaches infinite, which corresponds to a Fabry-Perot BIC [59–62].

To investigate this BIC, we select the distances between two gratings as $d = 470$, 480, and 490 nm. The corresponding phase shift between two gratings are $k_0d = 1.904\pi$, 1.944π, and 1.985π, respectively. According to the RCWA, we calculate the corresponding reflectance spectra (zero-order diffraction) of the coupled-grating systems for TE polarization at normal incidence, as shown by the blue solid lines in Figs. 9(a)–9(c). The corresponding fitted reflectance spectra based on the HCM [Eq. (8)] are also shown by the red dashed lines. As demonstrated, the reflectance spectra predicted by the HCM basically agree with those calculated by the RCWA. For $d = 470$, 480, and 490 nm, the fitted near- and far-field coupling strengths are ($\kappa = -0.0004 \times 10^{15}$ Hz, $\gamma_0 e^{-i\varphi} = \gamma_0 e^{-1.921\pi i}$), ($\kappa = -0.0001 \times 10^{15}$ Hz, $\gamma_0 e^{-i\varphi} = \gamma_0 e^{-1.953\pi i}$), and ($\kappa = -0.0001 \times 10^{15}$ Hz, $\gamma_0 e^{-i\varphi} = \gamma_0 e^{-1.995\pi i}$),

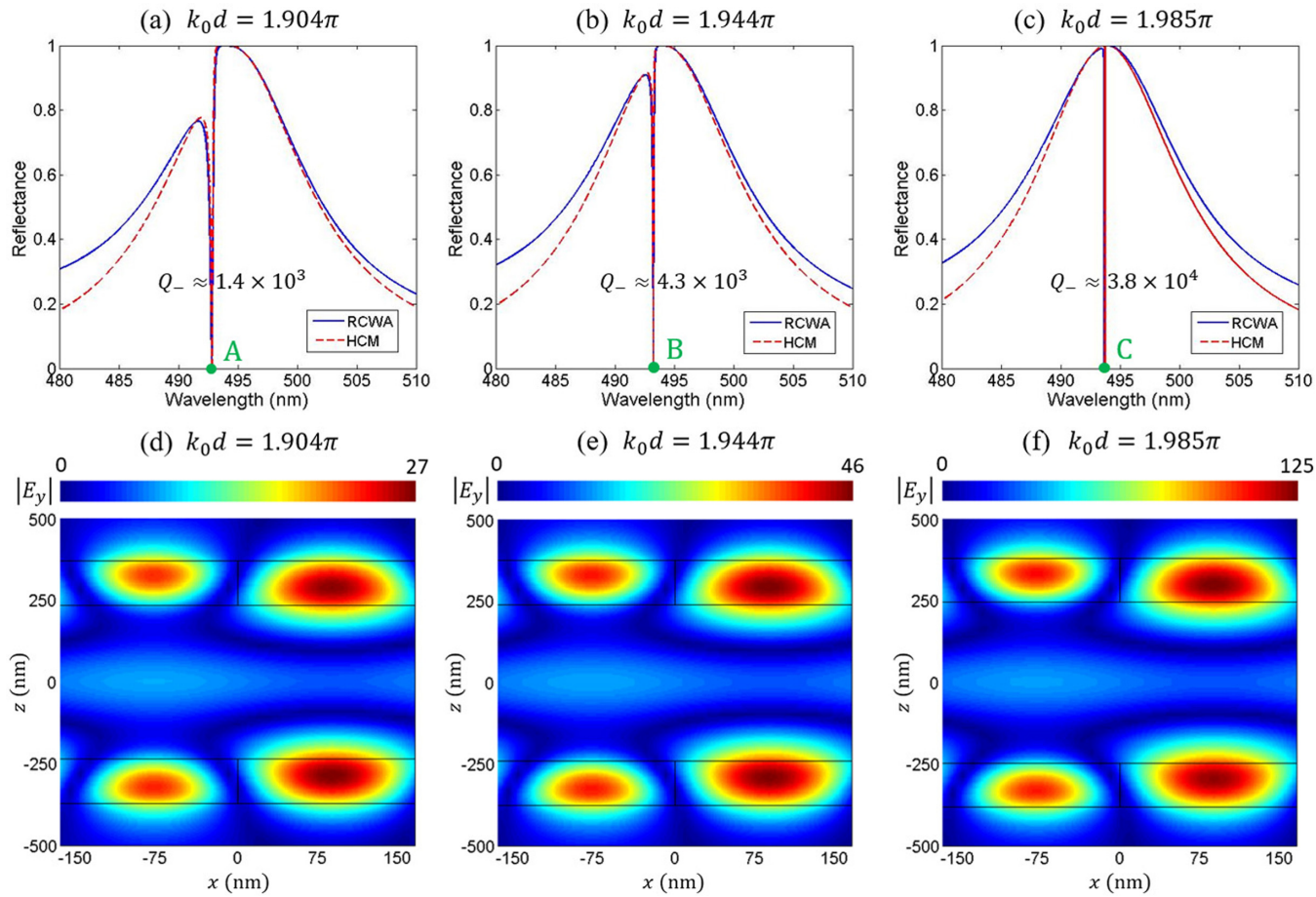

FIG. 9. Reflectance spectra of the coupled-grating systems with phase shifts between two gratings (a) $k_0d = 1.904\pi$, (b) $k_0d = 1.944\pi$, and (c) $k_0d = 1.985\pi$ for transverse electric (TE) polarization at normal incidence. Blue solid lines represent the reflectance spectra calculated by the rigorous coupled-wave analysis (RCWA). Red dashed lines represent the fitting reflectance spectra based on the hybrid coupling model (HCM). (d)–(f) Electric field intensity distributions $|E_y|$ at the corresponding reflectance dips (A–C). The incident electric field intensity is set to be unity, i.e., $|E_y^{\text{inc}}| = 1$.

respectively. It should be noted that the values of fitted near-field coupling strengths κ are not accurate since they are quite near zero (i.e., $\kappa \approx 0$) as two gratings are quite far away. As the phase shift gradually increases from 1.904π to 1.985π, the Q factor of the resonant mode Q_- rapidly increases from 1.4×10^3 to 3.8×10^4. Since $\kappa \approx 0$ and $\sin\varphi < 0$, the angular frequency positions of the resonant modes $\text{Re}(\omega_+)$ are smaller than those of the resonant modes $\text{Re}(\omega_-)$, according to Eq. (12a). Using the FDTD method, we simulate the electric field intensity distributions $|E_y|$ at the corresponding reflectance dips (A–C), as respectively shown in Figs. 9(d)–9(f). The incident electric field intensity is set to be unity, i.e., $|E_y^{\text{inc}}| = 1$. One can see that the electric field is greatly enhanced within the gratings. As the phase shift gradually increases from 1.904π to 1.985π, the maximum electric field intensity rapidly increases from ~27 to ~125, which indicates that the strength of the resonance increases dramatically.

Then we give the dependence of the Q factor of the resonant mode Q_- on the phase shift k_0d, as shown in Fig. 10. One can clearly see that, as the phase shift approaches 2π, the Q factor increases dramatically. For example, the Q factor reaches 3.5×10^5 when the phase shift is 1.999π. Therefore, the Q factor becomes infinite when the phase shift is equal to 2π, which is consistent with the theoretical prediction of

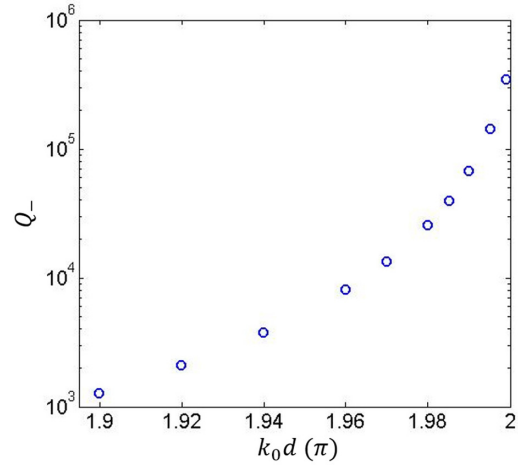

FIG. 10. Dependence of the Q factor of the resonant mode Q_- on the phase shift between two gratings k_0d.

Eq. (18b). Based on the HCM containing both near- and far-field couplings, the formation of the Fabry-Perot BICs can be explained clearly.

IV. CONCLUSIONS

In summary, we establish a HCM containing both near- and far-field couplings to describe the electromagnetic response of the coupled-grating system composed of two parallelly aligned subwavelength dielectric gratings. The HCM shows that the frequency positions of two resonant modes are determined by both near- and far-field coupling strengths, while the linewidths of two resonant of two resonant modes are completely determined by the far-field coupling strength. Through changing the distance between two dielectric gratings, both near- and far-field coupling strengths can be flexibly tuned, giving rise to rich electromagnetic responses. Additionally, the mechanism of the Fabry-Perot BICs in coupled-grating systems can be explained clearly by the HCM. These results show that the coupled-grating system is an effective platform to tailor electromagnetic responses.

ACKNOWLEDGMENTS

This paper is sponsored by the National Key Research Program of China (Grant No. 2021YFA1400602), the National Natural Science Foundation of China (Grants No. 12104105, No. 91850206, No. 11974261, No. 61621001, No. 11947065, No. 11704419, and No. 12104342), the Science Foundation of Shanghai (Grants No. 17ZR1443800 and No. 18ZR1442800), the Shanghai Science and Technology Committee (Grant No. 18JC1410900), the Natural Science Foundation of Jiangxi Province (Grant No. 20202BAB211007), the Start-up Funding of Guangdong Polytechnic Normal University (Grant No. 2021SDKYA033), and the Interdisciplinary Innovation Fund of Nanchang University (Grant No. 2019-9166-27060003). F.W. would like to thank a late mathematician engaged in the Goldbach conjecture, Jingrun Chen, for his tenacious spirit of exploration.

[1] A. E. Miroshnichenko, S. Flach, and Y. Kivshar, Fano resonances in nanoscale structures, Rev. Mod. Phys. **82**, 2257 (2010).

[2] S. A. Mann and A. Alù, Broadband Topological Slow Light Through Brillouin Zone Winding, Phys. Rev. Lett. **127**, 123601 (2021).

[3] M. Günay, A. Cicek, N. Korozlu, A. Bek, and M. E. Tasgin, Fano enhancement of unlocalized nonlinear optical process, Phys. Rev. B **104**, 235407 (2021).

[4] W. Liu, Y. Li, H. Jiang, Z. Lai, and H. Chen, Controlling the spectral width in compound waveguide grating structures, Opt. Lett. **38**, 163 (2013).

[5] Z. Wang, B. Zhang, and H. Deng, Dispersion Engineering for Vertical Microcavities Using Subwavelength Gratings, Phys. Rev. Lett. **114**, 073601 (2015).

[6] C. W. Hsu, B. Zhen, A. D. Stone, J. D. Joannopoulos, and M. Soljačić, Bound state in the continuum, Nat. Rev. Mater. **1**, 16048 (2016).

[7] A. F. Sadreev, Interference traps waves in an open system: Bound states in the continuum, Rep. Prog. Phys. **84**, 055901 (2021).

[8] S. Joseph, S. Pandey, S. Sarkar, and J. Joseph, Bound states in the continuum in resonant nanostructures: An overview of engineered materials for tailored applications, Nanophotonics **10**, 4175 (2021).

[9] Y. Shen, D. Ye, L. Wang, I. Celanovic, L. Ran, J. D. Joannopoulos, and M. Soljačić, Metamaterial broadband angular selectivity, Phys. Rev. B **90**, 125422 (2014).

[10] H. Deng, Z. Li, L. Stan, D. Rosenmann, D. Czaplewski, J. Gao, and X. Yang, Broadband perfect absorber based on one ultrathin layer of refractory metal, Opt. Lett. **40**, 2592 (2015).

[11] S. Xiao, T. Liu, X. Wang, X. Liu, and C. Zhou, Tailoring the absorption bandwidth of graphene at critical coupling, Phys. Rev. B **102**, 085410 (2020).

[12] F. Wu, D. Liu, and S. Xiao, Bandwidth-tunable near-infrared perfect absorption of graphene in a compound grating waveguide structure supporting quasi-bound states in the continuum, Opt. Express **29**, 41975 (2021).

[13] K. Kim and K. Om, Multiband photonic topological valley-Hall edge modes and second-order corner states in square lattices, Adv. Opt. Mater. **9**, 2001865 (2021).

[14] F. Wu, M. Luo, J. Wu, C. Fan, X. Qi, Y. Jian, D. Liu, S. Xiao, G. Chen, H. Jiang, Y. Sun, and H. Chen, Dual quasibound states in the continuum in compound grating waveguide structures for large positive and negative Goos-Hänchen shifts with perfect reflection, Phys. Rev. A **104**, 023518 (2021).

[15] Y. Cai, Y. Huang, K. Zhu, and H. Wu, Symmetric metasurface with dual band polarization-independent high-Q resonances governed by symmetry-protected BIC, Opt. Lett. **46**, 4049 (2021).

[16] Y. Akahane, T. Asano, B. Song, and S. Noda, High-Q photonic nanocavity in a two-dimensional photonic crystal, Nature (London) **425**, 944 (2003).

[17] X. Gan, H. Clevenson, and D. Englund, Polymer photonic crystal nanocavity for precision strain sensing, ACS Photonics **4**, 1591 (2017).

[18] W. Bogaerts, P. De Heyn, T. Van Vaerenbergh, K. De Vos, S. K. Selvaraja, T. Claes, P. Dumon, P. Bienstman, D. Van Thourhout, and R. Baets, Silicon microring resonators, Laser Photon. Rev. **6**, 47 (2012).

[19] H. Hodaei, M. Miri, M. Heinrich, D. N. Christodoulides, and M. Khajavikhan, Parity-time-symmetric microring lasers, Science **346**, 975 (2014).

[20] C. Ciracì, E. Poutrina, M. Scalora, and D. R. Smith, Origin of second-harmonic generation enhancement in optical split-ring resonators, Phys. Rev. B **85**, 201403(R) (2012).

[21] L. Smith, V. Shiran, W. Gomaa, and T. Darcie, Characterization of a split-ring-resonator-loaded transmission line at terahertz frequencies, Opt. Express **29**, 23282 (2021).

[22] N. Yu, P. Genevet, M. A. Kats, F. Aieta, J. Tetienne, F. Capasso, and Z. Gaburro, Light propagation with phase discontinuities:

Generalized lows of reflection and refraction, Science **334**, 333 (2011).
[23] S. Sun, Q. He, S. Xiao, Q. Xu, X. Li, and L. Zhou, Gradient-index meta-surfaces as a bridge linking propagating waves and surface waves, Nat. Mater. **11**, 426 (2012).
[24] S. Chen, W. Liu, Z. Li, H. Cheng, and J. Tian, Metasurface-empowered optical multiplexing and multifunction, Adv. Mater. **32**, 1805912 (2020).
[25] Z. S. Liu, S. Tibuleac, D. Shin, P. P. Young, and R. Magnusson, High-efficiency guided-mode resonance filter, Opt. Lett. **23**, 1556 (1998).
[26] F. Wu, J. Wu, Z. Guo, H. Jiang, Y. Sun, Y. Li, J. Ren, and H. Chen, Giant Enhancement of the Goos-Hänchen Shift Assisted by Quasibound States in the Continuum, Phys. Rev. Appl. **12**, 014028 (2019).
[27] J. K. S. Poon, J. Scheuer, Y. Xu, and A. Yariv, Designing coupled-resonator optical waveguide delay lines, J. Opt. Soc. Am. B **21**, 1665 (2004).
[28] D. Leykam, S. Mittal, M. Hafezi, and Y. D. Chong, Reconfigurable Topological Phases in Next-Nearest-Neighbor Coupled Resonator Lattices, Phys. Rev. Lett. **121**, 023901 (2018).
[29] B. Peng, Ş. K. Özdemir, S. Rotter, H. Yilmaz, M. Liertzer, F. Monifi, C. M. Bender, F. Nori, and L. Yang, Loss-induced suppression and revival of lasing, Science **346**, 328 (2014).
[30] C. Wang, W. R. Sweeney, A. D. Stone, and L. Yang, Coherent perfect absorption at an exceptional point, Science **373**, 1261 (2021).
[31] Y. Sun, W. Tan, H. Li, J. Li, and H. Chen, Experimental Demonstration of a Coherent Perfect Absorber with Pt Phase Transition, Phys. Rev. Lett. **112**, 143903 (2014).
[32] H. Li, S. Liu, S. Liu, S. Wang, H. Zhang, B. Bian, and X. Kong, Electromagnetically induced transparency with large delay-bandwidth product induced by magnetic resonance near field coupling to electric resonance, Appl. Phys. Lett. **106**, 114101 (2015).
[33] M. S. Sidorenko, O. N. Sergaeva, Z. F. Sadrieva, C. Roques-Carmes, P. S. Muraev, D. N. Maksimov, and A. A. Bogdanov, Observation of an Accidental Bound State in the Continuum in a Chain of Dielectric Disks, Phys. Rev. Appl. **15**, 034041 (2021).
[34] M. Airi and A. Alù, Exceptional points in optics and photonics, Science **363**, 42 (2019).
[35] K. Zhu, Y. Sun, J. Ren, and H. Chen, Loss revives bistable state near the exceptional point in a non-Hermitian microwave photonic meta-molecule, New J. Phys. **19**, 063043 (2017).
[36] C. Xu, W. E. Hayenga, H. Hodaei, D. N. Christodoulides, M. Khajavikhan, and P. LiKamWa, Enhanced modulation characteristics in broken symmetric coupled microring lasers, Opt. Express **28**, 19608 (2020).
[37] S. Han, R. Singh, L. Cong, and H. Yang, Engineering the Fano resonance and electromagnetically induced transparency in near-field coupled bright and dark metamaterial, J. Phys. D: Appl. Phys. **48**, 035104 (2015).
[38] P. Pitchappa, M. Manjappa, C. P. Ho, R. Singh, N. Singh, and C. Lee, Active control of electromagnetically induced transparency analog in terahertz MEMS metamaterial, Adv. Opt. Mater. **4**, 541 (2016).
[39] S. Zhang, D. A. Genov, Y. Wang, M. Liu, and X. Zhang, Plasmon-Induced Transparency in Metamaterials, Phys. Rev. Lett. **101**, 047401 (2008).
[40] W. Cao, R. Singh, C. Zhang, J. Han, M. Tonouchi, and W. Zhang, Plasmon-induced transparency in metamaterials: Active near field coupling between bright superconducting and dark metallic mode resonators, Appl. Phys. Lett. **103**, 101106 (2013).
[41] R. D. Kekatpure, E. S. Barnard, W. Cai, and M. L. Brongersma, Phase-Coupled Plasmon-Induced Transparency, Phys. Rev. Lett. **104**, 243902 (2010).
[42] H. Lu, X. Liu, D. Mao, and G. Wang, Plasmonic nanosensor based on Fano resonance in waveguide-coupled resonators, Opt. Lett. **37**, 3780 (2012).
[43] W. Zhu, Y. Ding, J. Ren, Y. Sun, Y. Li, H. Jiang, and H. Chen, Zak phase and band inversion in dimerized one-dimensional locally resonant metamaterials, Phys. Rev. B **97**, 195307 (2018).
[44] L. Gu, L. Fang, H. Fang, J. Li, J. Zheng, J. Zhao, Q. Zhao, and X. Gan, Fano resonance lineshapes in a waveguide-microring structure enabled by an air-hole, APL Photonics **5**, 016108 (2020).
[45] N. Kaina and R. Fleury, Hermitian formulation of multiple scattering induced topological phases in metamaterial crystals, Phys. Rev. B **102**, 134303 (2020).
[46] Z. Chen, Y. Zhou, and J. Shen, Photon antibunching and hunching in a ring-resonator waveguide quantum electrodynamics system, Opt. Lett. **41**, 3313 (2016).
[47] Z. Chen, Y. Zhou, and J. Shen, Dissipation-induced photonic-correlation transition in waveguide-QED systems, Phys. Rev. A **96**, 053805 (2017).
[48] B. Gallinet and O. J. F. Martin, Relation between near-field and far-field properties of plasmonic Fano resonance, Opt. Express **19**, 22167 (2011).
[49] X. Wang, P. Gogol, E. Cambril, and B. Palpant, Near- and far-field effects on the plasmon coupling in gold nanoparticle arrays, J. Phys. Chem. C **116**, 24741 (2012).
[50] W. Tan, Y. Sun, Z. Wang, and H. Chen, Manipulating electromagnetic responses of metal wires at deep subwavelength scale via both near- and far-field couplings, Appl. Phys. Lett. **104**, 091107 (2014).
[51] J. W. Rao, Y. T. Zhao, Y. S. Gui, X. L. Fan, D. S. Xue, and C.-M. Hu, Controlling Microwaves in Non-Hermitian Metamaterials, Phys. Rev. Appl. **15**, L021003 (2021).
[52] C. Fan, X. Shi, F. Wu, Y. Li, H. Jiang, Y. Sun, and H. Chen, Photonic topological transition in dimerized chains with the joint modulation of near-field and far-field couplings, Photon. Res. **10**, 41 (2022).
[53] Z. Chen, Y. Zhou, and J. Shen, Exact dissipation model for arbitrary photonic Fock state transport in waveguide QED system, Opt. Lett. **42**, 887 (2017).
[54] Z. Chen, Y. Zhou, and J. Shen, Entanglement-preserving approach for reservoir-induced photonic dissipation in waveguide QED system, Phys. Rev. A **98**, 053830 (2018).
[55] S. Tibuleac and R. Magnusson, Reflection and transmission guided-mode resonance filters, J. Opt. Soc. Am. A **14**, 1617 (1997).
[56] Y. Zhou, M. Moewe, J. Kern, M. C. Y. Huang, and C. J. Chang-Hasnain, Surface-normal emission of a high-Q resonator using a subwavelength high-contrast grating, Opt. Express **16**, 17282 (2008).
[57] S. Menon, A. Prosad, A. S. Lal Krishna, R. Biswas, and V. Raghunathan, Resonant mode engineering in silicon compatible

multilayer guided-mode resonance structures under Gaussian beam excitation condition, J. Opt. **23**, 105001 (2021).

[58] S. Fan, W. Suh, and J. D. Joannopoulos, Temporal coupled-mode theory for the Fano resonance in optical resonators, J. Opt. Soc. Am. A **20**, 569 (2003).

[59] H. Xu and Y. Shi, Silicon-waveguide-integrated high-quality metagrating supporting bound state in the continuum, Laser Photon. Rev. **14**, 1900430 (2020).

[60] H. Hemmati and R. Magnusson, Resonant dual-grating metamembranes supporting spectrally narrow bound states in the continuum, Adv. Opt. Mater. **7**, 1900754 (2019).

[61] D. C. Marinica, A. G. Borisov, and S. V. Shabanov, Bound States in the Continuum in Photonics, Phys. Rev. Lett. **100**, 183902 (2008).

[62] E. N. Bulgakov, D. N. Maksimov, P. N. Semina, and S. A. Skorobogatov, Propagating bound states in the continuum in dielectric gratings, J. Opt. Soc. Am. B **35**, 1218 (2018).

[63] L. Gu, H. Fang, J. Li, L. Fang, S. J. Chua, J. Zhao, and X. Gan, A compact structure for realizing Lorentzian, Fano and electromagnetically induced transparency resonance lineshapes in a microring resonator, Nanophotonics **8**, 841 (2019).

[64] J. Wang, A. Chen, Y. Zhang, J. Zeng, Y. Zhang, X. Liu, L. Shi, and J. Zi, Manipulating bandwidth of light absorption at critical coupling: An example of graphene integrated with dielectric photonic structure, Phys. Rev. B **100**, 075407 (2019).

[65] M. G. Moharam, D. A. Pommet, E. B. Grann, and T. K. Gaylord, Stable implementation of the rigorous coupled-wave analysis for surface-relief gratings: Enhanced transmittance matrix approach, J. Opt. Soc. Am. A **12**, 1077 (1995).

[66] F. Li, Use of Fourier series in the analysis of discontinuous periodic structures, J. Opt. Soc. Am. A **13**, 1870 (1996).

[67] Y. Zhang, W. Liu, Z. Li, Z. Li, H. Cheng, S. Chen, and J. Tian, High-quality-factor multiple Fano resonances for refractive index sensing, Opt. Lett. **43**, 1842 (2018).